Real-space Imaging of the Multiple Halogen Bonds by Ultrahigh-resolution Scanning Probe Microscopy

Dingguan Wang[1], Zishen Wang[1], Wei Liu[2], Arrame[1,3], Siying Zhong[1], Andrew T. S. Wee[1]*

[1]Department of Physics, National University of Singapore, 2 Science Drive 3, Singapore 117551, Singapore

[2]School of Physics, Southeast University, 2 Southeast University road, Nanjing, China

[3]Agency for Science, Technology and Research (A*STAR), Institute of Materials Research and Engineering (IMRE), 2 Fusionopolis Way, Innovis #08-03, Singapore 138634

*Correspondence and requests for materials should be addressed to Prof. A. T. S. Wee (E-mail: phyweets@nus.edu.sg)

ABSTRACT: Understanding the physical origin of STM/AFM image contrast is of significance for not only promoting surface characterization techniques, but also probing surface nanostructures with the atomic/sub-molecular resolution. Herein, we demonstrate the real-space imaging of halogen bonds acquired by non-contact atomic force microscopy (nc-AFM)/bond-resolution scanning tunneling microscopy (BR-STM) with functional CO-tip, and study the image contrast origin of halogen bonds. The presence of bright line features is associated to the specific site where halogen bond forms, which is experimentally evidenced to be contributed by both CO-tip bending and electron density exchange. Three distinct types of halogen bonds are observed, which origin from the noncovalent interactions of Br-atoms with positive potential H-atom, neutral potential Br-atom and negative potential N-atom, respectively. Our work shows that nc-AFM and BR-STM can directly image halogen bonds and can be used to unambiguously discriminate their bonding

features. This work demonstrates the potential use of this technique to image other non-covalent intermolecular bonds and to understand complex supramolecular assemblies at the sub-molecular level.

Introduction

The chemical bond is of central interest in the chemistry discipline, and it plays an important role in the construction of both matter and life. In particular, non-covalent bonds are the fundamental basis of supramolecular self-assembly,[1] including hydrogen bonds,[2] halogen bonds,[3] coordination bonds,[4, 5] dipole-dipole interactions[6] and so on.[7-9] The halogen bond has recently attracted much interest,[10] while the hydrogen bond has been the most studied intermolecular interaction in the past.[11, 12] Halogen bonds form mainly through the mutual interaction between halogen atoms (e.g. F, Cl, Br, I) due to the coexistence of both positive and negative potential centers at the halogen atom caused by its asymmetrical electron distribution.[13, 14] Recent research has discovered that halogen atoms also interact with other non-halogen elements (e.g. S and O elements) to form a halogen bond,[15-18] which further enriches the database of halogen bonds. The study of halogen bonds is useful not only to understand the internal mechanism of supramolecular self-assembly at the molecular level, but also to develop functional nanomaterials constructed via halogen bonds. On-surface supramolecular self-assembly based on halogen bonds has also attracted much interest.[10, 16] By employing halogen bonding, various ordered supramolecular structures have been reported, such as two-dimensional porous networks,[19] Sierpiński triangle Fractals.[20]

Over the past decades, both scanning tunneling microscope (STM) and atomic force microscopy (AFM) have been employed to study various surface structures, molecular assembly and on-surface reactions.[21, 22] However, the realization of atomic-resolution molecular structures

is challenging for the conventional AFM and STM technique. The invention of qPlus AFM sensor greatly improves the resolution of AFM image and resolves the atomic structure within a single molecule.[23, 24] A metallic tip modified with functional molecules (most commonly CO-tip) further improves the AFM resolution.[25] Leo *et al.* has demonstrated the chemical structure of a single pentacene molecule resolved using qPlus atomic force microscopy (or nc-AFM) with CO-tip.[26] The similar technique can also be applied for the internal chemical structure and bond-order discrimination.[27-30] Moreover, qPlus-AFM can also be used for direct imaging of the intermolecular hydrogen bond.[31] For example, Zhang *et al.* reported in 2013 a real-space image of the hydrogen bond formed in 8-hydroxyquinoline clusters using noncontact atomic force microscopy (nc-AFM) with CO-tip, although the origin of the hydrogen bond remains controversial.[32] It is worth noting that functional tip also greatly improves the resolution of the STM image. In recent years, several reports have shown that STM with CO-tip is also able to unravel the internal atomic structure of a single molecule.[33-35] The intermolecular force of triangular halogen bonds has also recently been studied by nc-AFM and STM,[36] and the bright lines appear at positions where the triangular halogen bond form at STM images.[13] The bright lines (or image contrast) are thought to originate from the interacting electrons of intermolecular bonds, while others propose that bright lines are caused by the bending of the CO molecule.[37, 38] Currently, the origin of the bright line is still controversial, and understanding the origin of the bright line (image contrast) is not only conducive to the understanding of non-covalent bonds, but also of great significance to the improvement of this surface characterization technique. Furthermore, there are many other forms of halogen bonds other than the reported triangular halogen bond, and more details of halogen bonds need to be carefully studied by ultrahigh-resolution STM and nc-AFM.[36]

In this work, we present the diversity of halogen bonds, including tetragonal Br-Br bonds, Br-N bond and Br-H bond, and directly image them using nc-AFM and BR-STM. A nitrogen-doped and bromine-terminated 2-TBQP molecule was synthesized and deposited on Au(111) substrate to obtain the self-assembled molecular clusters. At low molecular coverage, two distinct forms of 2-TBQP dimers are observed. Nc-AFM images the real-space atomic structure of the 2-TBQP molecule. Moreover, two different types of Br-N bonds (namely type-1 and type-2 Br-N halogen bonds) are observed in the two forms of 2-TBQP dimers, respectively, verified by the presence of bright lines between two corresponding atoms (Br-H and Br-N atoms). Density functional theory (DFT) calculations shows that there is obvious electron density redistribution between the adjacent Br-N and Br-H atoms, suggesting that the halogen bonds are essentially electrostatic interactions. At high molecular coverage, we observe the formation of a 2-TBQP tetramer. Both nc-AFM and BR-STM directly image the formation of tetragonal halogen bonds on top of the 2-TBQP tetramer, appearing as tetragonal bright lines that link four Br-atoms. By contrast, no bright line is observed between two adjacent but no-bonding Br-atoms even though the tip-sample distances are close.

Results

Atomic structure and electrostatic potential of a single 2-TBQP molecule. Figure 1 displays atomic structure and electrostatic potential of 2, 7, 13, 18-tetrabromodibenzo[a,c]dibenzo [5,6:7,8]-quinoxalino[2,3-i]-phenazine (2-TBQP). The 2-TBQP molecule was synthesized following previous work.[21, 39] Figure 1a shows its atomic structure obtained from single crystal XRD. 2-TBQP molecule is a planar π-conjugated polycyclic hydrocarbon with four doping nitrogen atoms (red atoms) and four bromine atom terminals (blue atoms). 2-TBQP molecules were deposited on a clean Au(111) crystal substrate held at room temperature, and the as-prepared samples were then transferred *in-situ* into LT-STM/nc-AFM chamber for imaging at 4.2 K. Figure

1b presents an atomic resolution nc-AFM image of a single 2-TBQP molecule on Au(111) acquired with a CO-modified tip. The nc-AFM molecular image structure is experimentally reproducible. Nine benzene rings are observed with four bright spots at its terminals, corresponding to the four Br-atoms. We infer that the Br-atoms exhibit higher frequency shift (Δf) due to its larger atom size than the other element atoms, indicating stronger interaction of the Br-atom to CO-tip at a given tip-sample distance. In contrast, the N-atom sites have low Δf intensity and the N-containing benzene ring becomes larger compared to atomic structure shown in Figure 1a. The distinct Δf contrasts in the nc-AFM image may be due to the variable van der Waals (vdW) interactions between CO-tip and element atoms.[40]
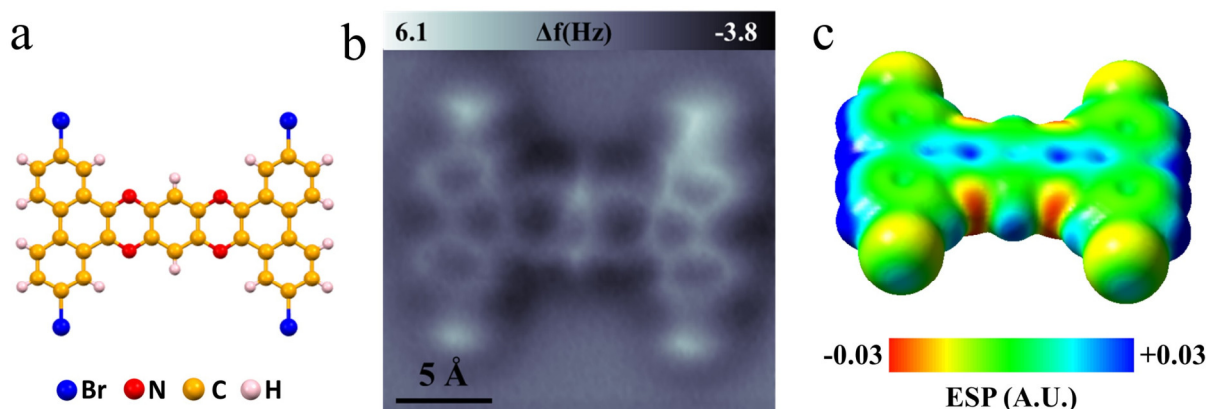

Figure 1. Atomic structure and electrostatic potential of a single 2-TBQP molecule. (a) Atomic structure of 2-TBQP molecule. (b) Atomic resolution nc-AFM image of a single 2-TBQP molecule on Au(111) acquired with a CO-modified tip, set-point: V = 50 mV, I = 20 pA, tip height Z = -0.1 Å and oscillation amplitude A = 40 pm. (c) Electrostatic potential (ESP) of a 2-TBQP molecule projected on an iso-surface of 0.001.

Figure 1c displays the calculated electrostatic potential (ESP) of a 2-TBQP molecule. The marked bar indicates the electrostatic potential intensity, where red represents negative

electrostatic potential while blue represents positive electrostatic potential. As expected, N-atom sites display a negative electrostatic potential, while H-atom sites have a positive electrostatic potential. Both negative and positive electrostatic potential are observed within a Br-atom due to the anisotropic distribution of halogen atom electron density. This electron anisotropic distribution leads to the coexistence of electron depleted δ-hole cap at the terminal of the C–Br bond (light blue) and encircling electron-rich belt perpendicular to the C–Br bond (yellow), in line with previous reports.[13, 15]

The formation of two distinct types of 2-TBQP dimers. Figure 2 displays two distinct forms of 2-TBQP dimers stabilized via two types of Br-N halogen bonds. Figure 2a shows an atomic resolution nc-AFM image of type-1 dimer. Two Br-atoms are observed to be adjacent to two N-atoms, respectively. An enlarged nc-AFM image in Figure 2b shows that one of the Br-atoms is adjacent to a N-atom of another 2-TBQP molecule. A bright line (labeled by a red arrow) between the Br-N atoms appears, suggesting the formation of Br-N bond (named as type-1 Br-N halogen bond). Three bright lines (labeled by blue arrows) are also observed at the vicinity of the Br-N bright line, which connects three series of Br-H atoms, respectively. We note that the intensity of Br-N bright line is somewhat lower than that of the Br-H bright lines. Figure 2c outlines a DFT-optimized molecular packing structure of type-1 dimer. According to the observed bright lines in nc-AFM image in Figure 2b, red and black dotted-lines are added in Figure 2c to connect Br-N atoms and Br-H atoms, respectively.
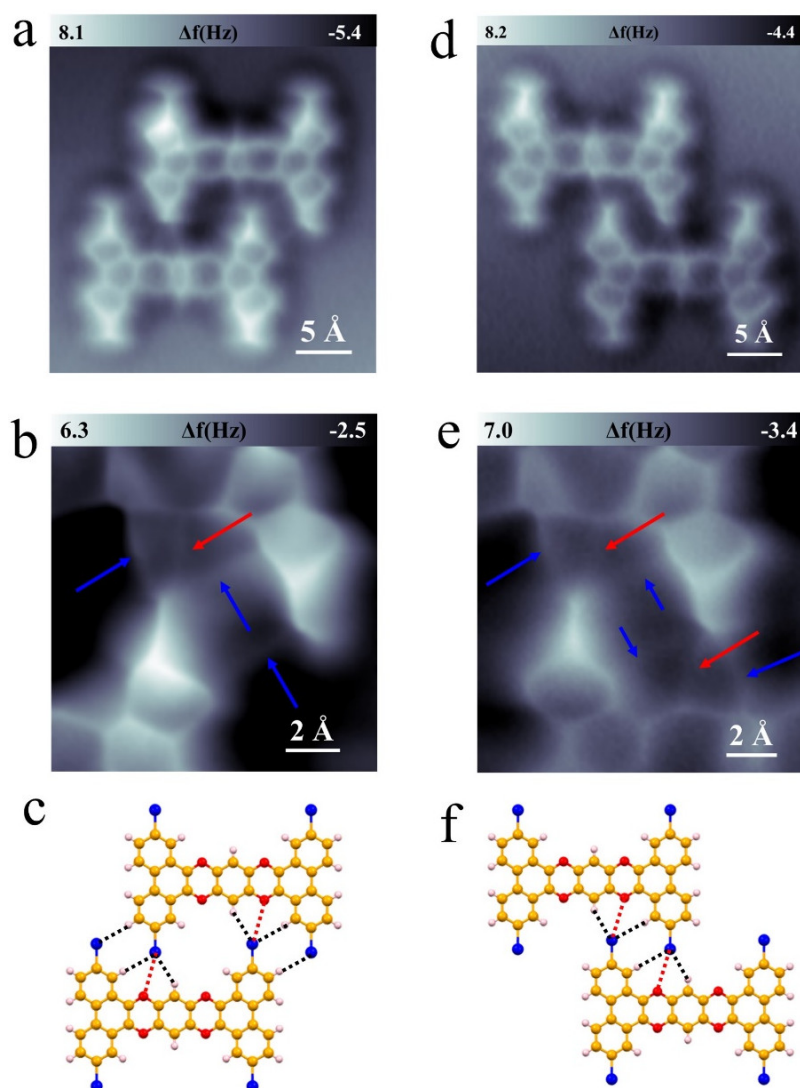
Figure 2. Two types of Br-N halogen bonds. (a) Atomic resolution nc-AFM image of type-1 dimer, set-point: V = 60 mV, I = 20 pA, tip height Z = 0.3 Å and oscillation amplitude A = 40 pm. (b) An enlarged nc-AFM image of type-1 dimer, set-point: V = 60 mV, I = 20 pA, tip height Z = -0.2 Å and oscillation amplitude A = 40 pm. (c) DFT-optimized molecular packing structure of type-1 dimer. (d) Atomic resolution nc-AFM image of type-1 dimer, set-point: V = 60 mV I = 20 pA, Z=0.3 Å and oscillation amplitude A = 60 pm. (e) An enlarged nc-AFM image of type-2 dimer, set-point: V = 60 mV, I= 20 pA, tip height Z = -0.1 Å and oscillation amplitude A = 40 pm. (f) DFT-optimized molecular packing structure of type-2 dimer. The red arrows label the bright lines

between Br-N atoms, and the blue arrows label the bright lines between Br-H atoms in (b and e), respectively; red dotted-lines and black dotted-lines indicate the formation Br-N and Br-H halogen bonds in (c and f), respectively.

Figure 2d shows a nc-AFM image of type-2 dimer. Like type-1 dimer, both Br-N and Br-H halogen bonds form in type-2 dimer although their molecular packing structure is different. A real-space atomic-resolution image in Figure 2e shows that two Br-atoms are adjacent to two N-atoms, respectively. Two bright lines (labeled by two red arrows) are observed to connect two couples of Br-N atoms, suggesting the formation of two Br-N bonds (named as type-2 Br-N halogen bond). In addition, another two bright lines (labeled by blue arrows) appear at the sides of each Br-N bright line, which connect two couples of Br-H atoms, respectively. Figure 2f presents a DFT-optimized molecular structure of type-2 dimer with red and black dotted-lines that connect Br-N atoms and Br-H atoms, respectively. According to the electrostatic potential of a 2-TBQP molecule in Figure 1c, we believe that the formation of a Br-N halogen bond results from the mutual interaction between an electron pair in N-atom and an electron depleted δ-hole at the terminal of the C–Br, and the formation of Br-H halogen bond arises from the interaction between the electron depleted H-atom and an encircling electron-rich belt at the Br-atom. We infer that the nc-AFM-observed bright lines origin from a synergistic effect of the exchange electron density of halogen bonds and the CO-tip bending, as further discussed in Figure 5.

To obtain more insight regarding the two types dimers, DFT calculations were carried out to determine the optimized molecular packing structure and their electron density difference. Figure 3a and 3b plot the calculated intermolecular interaction energy of type-1 and type-2 dimers as a function of Br-N distance, respectively. As expected, the interaction energy per molecule first decreases and then increases as the Br-N distances increase for both type-1 and type-2 dimers. The

Br-N bond distances at interaction energy minimization are 3.54 Å for type-1 dimer and 3.58 Å for type-2 dimer, respectively, which match well with the experimental measurements (3.45 ± 0.1 Å, labeled by red pentacles).
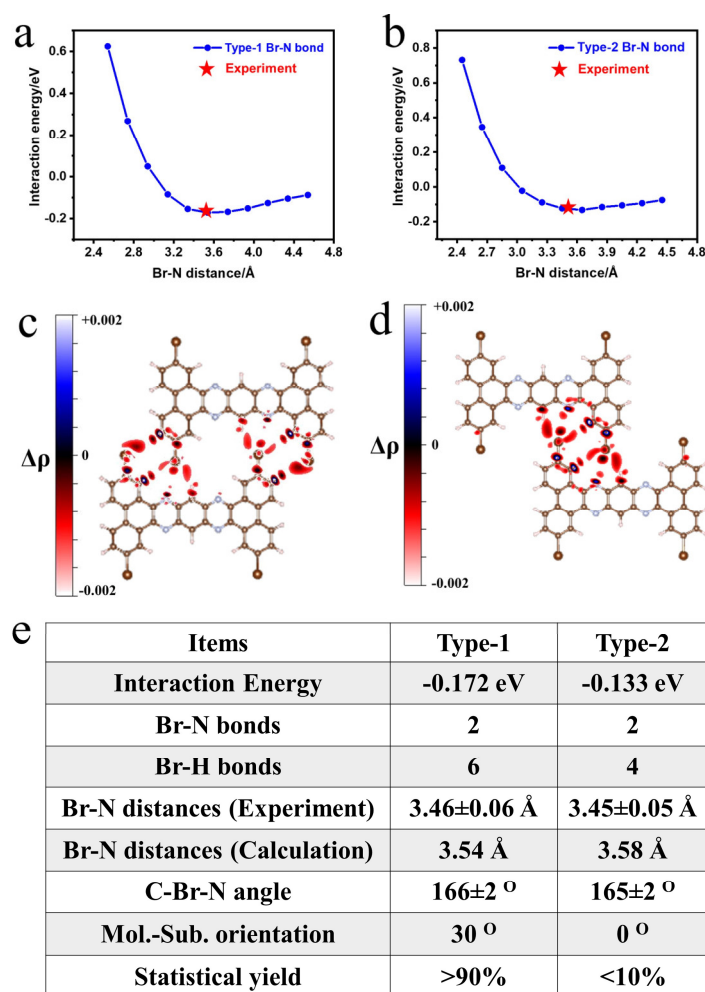
Figure 3. DFT calculations of two types of Br-N halogen bonds. (a, b) Calculated intermolecular interaction energy per molecule of type-1 dimer and type-2 dimer as a function of Br-N distance, respectively. (c, d) Calculated electron density difference ($\Delta\rho$) between two monomers and type-1 dimer/type-2 dimer, respectively. (e) Summary of the characters of the two Br-N halogen bonds obtained from experiment and DFT calculation.

Items	Type-1	Type-2
Interaction Energy	-0.172 eV	-0.133 eV
Br-N bonds	2	2
Br-H bonds	6	4
Br-N distances (Experiment)	3.46±0.06 Å	3.45±0.05 Å
Br-N distances (Calculation)	3.54 Å	3.58 Å
C-Br-N angle	166±2 °	165±2 °
Mol.-Sub. orientation	30 °	0 °
Statistical yield	>90%	<10%

DFT calculations were also carried out to obtain the electron density difference ($\Delta\rho$), which provides the intermolecular bonding features of Br-N and Br-H halogen bonds. Figure 3c and 3d show the charge density difference projected onto type-1 and type-2 dimers, respectively. Obvious electron density accumulation is observed at the connection of both Br-N atoms and Br-H atoms, suggesting the charge transfer between Br-atoms and N-atoms/H-atoms. Similar results of the charge transfer between Br-O atoms were also reported by Giovanni et al.[15] The formation of Br-N and Br-H halogen bonds is primarily electrostatic. The calculated results suggests that charge transfer between Br-N and Br-H atoms also play an important role, in line with IUPAC recommendations and literature reports.[3, 15, 41] We infer that the electron density between Br-N and Br-H atoms may also contribute to the bright lines feature observed at nc-AFM images in Figure 2b and 2e, and the higher intensity of electron density between Br-H atoms than that between Br-N atoms results in a brighter line of Br-H bond than that of Br-N bond shown at nc-AFM images. More details are discussed in Figure 5.

A significant difference is found in the proportion yield of the two types of 2-TBQP dimers, with a higher yield of type-1 than that of type-2. Statistically, the yield of type-1dimer is greater than 90%, while the yield of type-2 dimer is less than 10%. To explain the observed results, we summarize in Figure 3e the characters of Br-N halogen bonds, which include formation energy, the numbers of halogen bonds, bond distance and bond angle. Type-1 dimer has lower formation/interaction energy than type-2 dimer, and Figure 3e shows that the interaction energy are -0.172 eV and -0.133 eV for type-1 and type-2 dimer, respectively. The distinct interaction energy result from a difference in the bonding number of halogen bonds formed between type-1 and type-2 dimer. As show at the third row in Figure 3e, two Br-N intermolecular bonds form for both type-1 and -2 dimers. However, the fourth row in Figure 3e shows that type-1 dimer (6 Br-H

bonds) has more formed Br-H halogen bonds than that of type-2 dimer (4 Br-H bonds). We infer that the two additional Br-H bonds lead to a lower formation energy and thus a higher yield of type-1 dimer. Another distinct feature between the two dimers is the orientation of molecule with the Au[110] direction of Au substrate. Figure S2 shows that the relative orientations of molecule with respect to the Au[110] direction are 30 degree and 0 degree for type-1 and type-2 dimer, respectively. The calculated total absorption energy with substrate is -4035.95 eV and -4035.88 eV for the 30 degree case and the 0 degree case, respectively. The total energy difference is only -0.07 eV, and such a small energy difference suggests that the Au substrate does not play an important role in the formation of the dimers.

The bonding angle of the Br-N bond is also acquired. Unexpectedly, nc-AFM images in Figure 2b and 2e show that the Br atom does not align with two N-atoms of a pyrazine ring. The bond angle of the Br-N bond, measured along N-Br-C, is 166 ± 2 ° and 165 ± 2 ° for type-1 and type-2 dimers, respectively, which are close to but different from a theoretical bonding angle of 180 °. Similar bending halogen bond was reported by Ebeling *et al*.[36] We infer that the steric hindrance of two adjacent H-atoms hinders the alignment of Br-atom with two N-atoms of a pyrazine ring. The Br-atom optimises its position to enable the formation of both Br-N and Br-H halogen bonds, suggesting the flexible bonding angle of non-covalent halogen bonds, unlike rigid covalent bonds. We propose that the flexibility of non-covalent intermolecular bonds is one of the reasons why supramolecular structures form over a larger ordered area than the covalently linked network, besides the reversibility of the non-covalent bonds.[42]

Formation of 2-TBQP tetramer. Figure 4 displays another self-assembled structure of 2-TBQP tetramer stabilized by tetragonal Br-Br halogen bonds with assistance of Br-atoms absorption. The 2-TBQP tetramer are observed at a higher molecular coverage of 0.2 ML in Figure

S3. Figure 4a gives a STM image of the supramolecular structure of 2-TBQP tetramer on Au(111). The STM image displays the H-shaped molecular skeleton of a single 2-TBQP molecule. Individual Br-atoms (labeled by blue arrows) adsorb on the periphery of 2-TBQP molecules. The individual Br-atoms come from the partial Br-atom cleavage from 2-TBQP molecules at room temperature, and the evidence is presented in Figure S4. The formation of self-assembled 2-TBQP tetramer is observed, and four Br-atoms (labeled by blue quadrate) from four 2-TBQP molecules are adjacent and form a square geometric structure. We infer that the formation of tetragonal Br-Br halogen bonds governs the self-assembled 2-TBQP tetramer. To verify our hypothesis, nc-AFM measurements were carried out. Figure 4b shows a nc-AFM image of the 2-TBQP tetramer acquired using a CO-tip, which clearly shows their molecular atomic structure. Br-atoms are clearly imaged, and two kinds of Br-atoms are observed. The first kind is the individual Br-atoms (labeled by blue arrows) that cleave from 2-TBQP molecules, and the second kind is the Br-atom that remain bonded to 2-TBQP molecules (labeled by blue arrows). The individual Br-atoms are adjacent to N-atom sites (labeled by blue arrows in Figure 4b), suggesting a site-selective adsorption at the N-atom site for the individual Br-atom. The individual Br-atoms play an important role in the formation of the 2-TBQP tetramer rather than type-1 or -2 dimer. We infer that the adsorption of the individual Br-atom on the N-atom site prevents the formation of Br-N bonding type-1 & -2 dimers, thus leading to formation of 2-TBQP tetramer stabilized via tetragonal Br-Br halogen bonds. The evidence is presented in Figure S5, which displays that a 2-TBQP trimer is governed by the combination of Br-Br and Br-N halogen bonds. An individual Br-atom adsorbs on one of N-atom sites of the Br-N bonding type-1 dimer. Due to steric hindrance arisen by the individual Br-atom adsorption, the third 2-TBQP molecule joins to the type-1 dimer via Br-Br bond rather than Br-N bond.
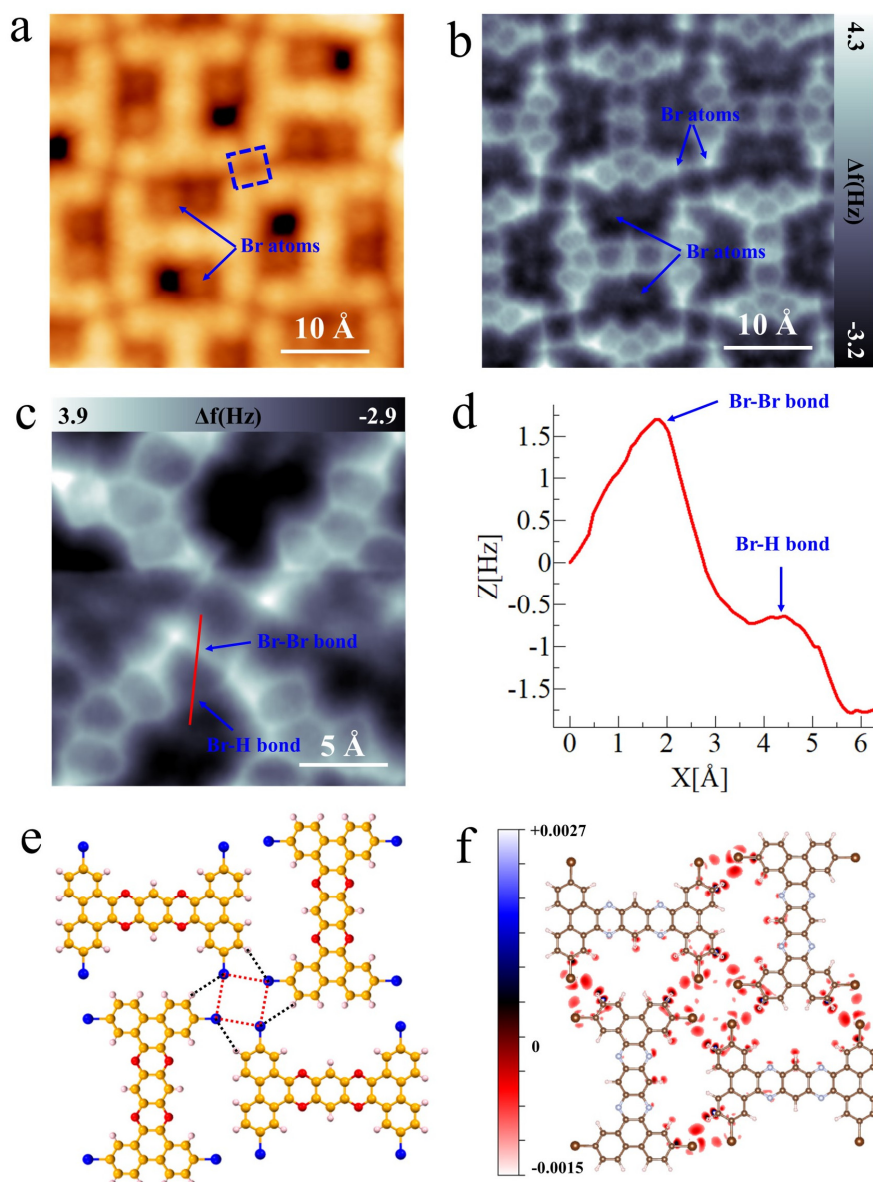
Figure 4. Formation of 2-TBQP tetramer stabilized by tetragonal Br-Br halogen bonds with assistance of Br-atoms absorption. (a) STM image (b) nc-AFM image of another self-assembled structure of 2-TBQP tetramer on Au(111), set point: a) V = 50 mV and I = 20 pA; b) V=50 mV I=20 pA, Z=0 Å and oscillation amplitude A = 60 pm; the blue arrows indicate the individual Br-atoms that are adjacent to nitrogen atom sites. (c) An enlarged nc-AFM image of tetragonal Br-Br halogen bonds and (d) its corresponding frequency shift profile of Br-Br and Br-H bonds, set-point:

V= 50 mV, I= 20 pA, tip height Z = -0.3 Å and oscillation amplitude A = 60 pm, the blue arrows indicate the bright lines between Br-Br atoms and Br-H atoms, respectively. (e) DFT-optimized molecular packing structure of the 2-TBQP tetramer stabilized by tetragonal Br-Br halogen bonds, red dotted-lines and black dotted-lines indicate the Br-Br and Br-H halogen bonds, respectively. (f) Calculated electron density difference ($\Delta\rho$) between four monomers and the 2-TBQP tetramer.

To clearly image the tetragonal Br-Br halogen bonds, a closer tip-sample distance was applied. Figure 4c displays an enlarged nc-AFM image of the 2-TBQP tetramer. Four obvious bright lines labeled as Br-Br bond (blue arrow) are observed to link pairs of two Br-atoms, verifying the formation of tetragonal Br-Br halogen bonds. Another kind of Br-H halogen bond also can be probed. As marked by a blue arrow with a label of "Br-H bond" in Figure 4c, an inconspicuous bright line at the side of the Br-Br bright line is also observed to link Br-H atoms. Figure 4d displays a frequency shift profile along the red line in Figure 4e across both the Br-Br and Br-H bright lines. The frequency shift profile shows two obvious peaks at the positions of both Br-Br and Br-H bright lines, respectively, indicating abrupt incremental changes in the signature of frequency shift. Figure 4e gives a DFT-optimized molecular packing structure of the 2-TBQP tetramer. The calculated Br-Br bond length and bond angle are 3.72 Å and 90 $^\circ$, respectively, and the calculated values are in agreement with the experimental values (3.70 $\pm$ 0.10 Å, 91 $\pm$ 2 $^\circ$). Thus, both nc-AFM measurements and DFT calculations verify that the formation of the 2-TBQP tetramer is stabilized via tetragonal Br-Br halogen bonds and Br-H halogen bonds. Red dotted-lines and black dotted-lines are added in Figure 4e to indicate the Br-Br and Br-H halogen bonds, respectively. Figure 4f displays the calculated electron density difference of the 2-TBQP tetramer. Obvious electron density exchange is observed between both Br-Br atoms and Br-H atoms, suggesting the charge transfer occurs across the Br-Br atoms and the Br-H atoms, similar to the

case of Br-N bond. We infer that the electron density can be probed by nc-AFM and contribute to the appearance of bright lines between Br-Br atoms and Br-H atoms.

The origin of bright line feature of halogen bonds. We note that similar bright line feature of intermolecular hydrogen bond was also imaged by nc-AFM with CO-tip by Xiaohui *et al*.[32] The appearance of bright line feature of hydrogen bond was explained to be contributed by the increased electron density at the hydrogen bond position, which enhances the Pauli repulsion between CO-tip and the hydrogen bond. However, Habala *et al.* found in their simulated calculations that a bright line feature of the intermolecular hydrogen bond could also be caused by the CO-tip bending.[38] Since no intermolecular electron density is involved in their simulated calculations, they claimed that CO-tip bending plays a major role in nc-AFM imaging of intermolecular hydrogen bond. Pavlicek *et al.* observed an apparent bond ridge (bright line) between two sulfur atoms of a DBTH molecule where no chemical bond forms.[43] Liljeroth *et al.* also observed experimentally a bright line in nc-AFM images between two N atoms that did not form an intermolecular chemical bond.[37] Therefore, their experiments suggest that CO-tip bending is a major factor in nc-AFM images. However, whether CO-tip bending or electron density plays a key role in imaging of intermolecular bond has not fully been determined.

We obtained both nc-AFM and BR-STM images of two adjacent Br-atoms with intermolecular bonding and the absence of chemical bonding, respectively. Figure 5 displays constant-height nc-AFM images (top row) and BR-STM images (bottom row) as the function of tip-sample heights (ΔZ). One can note that the Br-Br distances for the two cases are very close, and their measured Br-Br distances are 370 ± 10 pm and 345 ± 10 pm for intermolecular bonding case and non-bonding case, respectively. At $\Delta Z= + 0.2$ Å, no bright line feature is observed for the two cases in both nc-AFM and BR-STM images. As the CO-tip approaches to the sample, a bright line feature

in both nc-AFM and BR-STM images become more prominent for the intermolecular bonding case, while no bright line feature appears for the no bonding case. For example, at $\Delta Z < -0.2$ Å, an obvious bright line feature is observed between two Br-atoms where halogen bond forms (the intermolecular bonding case) in both nc-AFM and BR-STM images. In contrast, no bright line appears between two adjacent but individual Br-atoms where no bond forms (no bonding case) even at close tip-sample distance. These experimental observations verify that the formation of intermolecular halogen bond contribute to the appearance of bright line features, suggesting that the electron density play an important role in nc-AFM and BR-STM image contrasts. Sweetman *et al* have also reported that the bright line originated from the electron repulsion that occurs within the tip-sample junction based on a comparison of experimental images and force spectra.[31]
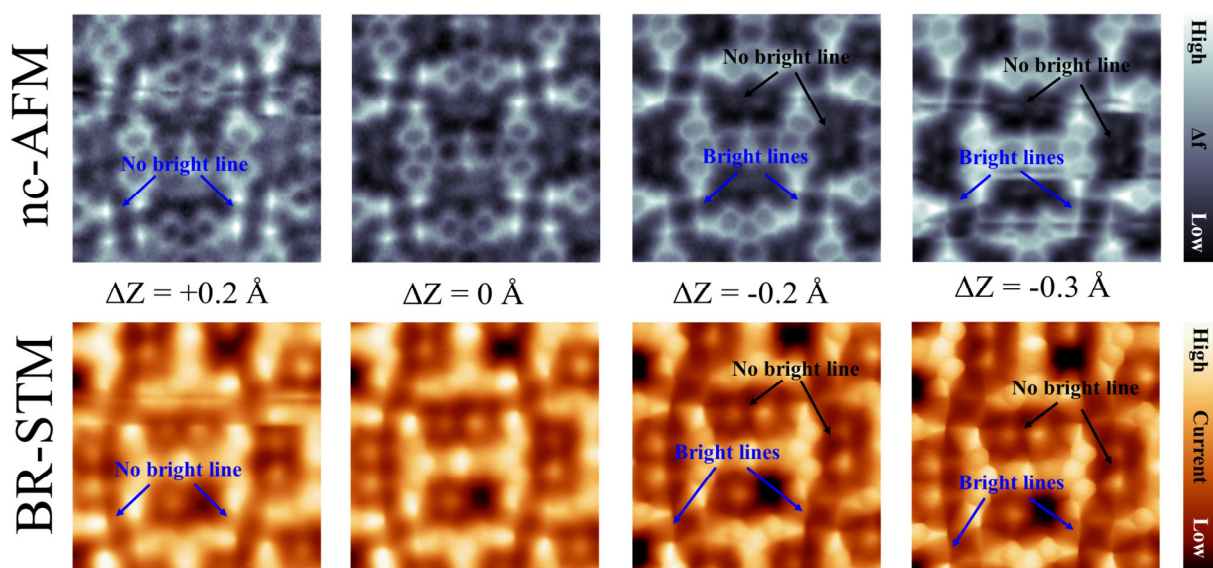
Figure 5. Imaging the intermolecular bonding and the absence of chemical bonding of two adjacent Br-atoms by nc-AFM and BR-STM. (Top row) Constant-height *nc*-AFM images with a CO-tip taken at different tip heights (ΔZ); four Br-Br intermolecular bright lines (labeled by blue arrows) are observed on top of the tetragonal Br-Br halogen bonds at close tip-sample distances,

while no bright line is observed between two adjacent but no-bonding Br-atoms (labeled by black arrows). (Bottom row) Bond-resolution constant-height STM (BR-STM) images with a CO-tip at the given heights (ΔZ); similarly, four bright lines (labeled by blue arrows) are observed on top of the tetragonal Br-Br halogen bonds, while no bright line is observed between two adjacent but no-bonding Br-atoms (label by black arrows) even at close tip-sample distances. Set point: top row) V = 50 mV and I = 20 pA, oscillation amplitude A = 60 pm; bottom row) V= 5-30 mV, I=20 pA; Size: 3 nm × 3 nm. The measured Br-Br distances are 370 ± 10 pm and 345 ± 10 pm for intermolecular bonding case and no bonding case, respectively.

Besides the contribution of electron density, we believe that the CO-tip bending also contributes to the bright line features based on the following two experimental observations. The first observation is that a gradual frequency shift peak also appears between the two non-bonding Br-atoms at close tip-sample distance in Figure S6, although no corresponding bright line is observed and its frequency shift intensity is much lower than that of two intermolecular bonding Br-atoms. The second observation is that the intensity of the bright lines is not proportional to the electron density (compared Br-Br bond with Br-H bond in Figure 4c and 4f), suggesting that not only electron density contributes to the bright line feature. At close tip-sample distance, CO-tip bending often occurs, evidenced by a disturbed line appearance and the observation of apparent sample drift in Figure S6. Considering of both our experimental observation and the other reported works by Pavlicek and Liljeroth *et al*,[37, 43] we believe that both CO-tip bending and electron density play key roles in imaging of intermolecular bond.

Conclusion

In conclusion, we demonstrated the physical origin and the diversity of halogen bonds in self-assembled 2-TBQP molecules on Au(111). The halogen bond was directly imaged as bright line

features by nc-AFM/BR-STM, and the bright line is contributed by a synergistic effect of CO-tip bending and electron density exchange, as evidenced by the experimental observation that bright lines are observed at two intermolecular bonding Br-atoms, whereas two adjacent but non-bonding Br-atoms do not display such lines. We observed three types of halogen bonds, namely the Br-H halogen bond, Br-Br halogen bond and Br-N halogen bond, suggesting the diverse class of halogen bonds results from its bonding environment; halogen atoms can interact with manifold element atoms of positive (H-atom), neutral (Br-atom) and negative (N-atom) potential. In addition, a bending Br-N halogen bond was observed with a bond angle of $\sim 165\,^{\circ}$ rather than theoretical bond angle of $180\,^{\circ}$, implies the flexibility of halogen bonds. This work demonstrates the versatility of combined nc-AFM/BR-STM in understanding halogen bonding, and further exploration of other intermolecular bonds using this technique is needed.

Methods

Synthesis of 2,7,13,18-tetrabromodibenzo[a,c] dibenzo[5,6:7,8]quinoxalino-[2,3-i]phenazine (2-TBQP). The 2-TBTBP molecule was synthesized according to the literature.[39] To confirm its structure, 2-TBQP powder was sublimed to obtain single crystals for single-crystal XRD analysis. CCDC 1455701 (2-TBQP) contains the supplementary crystallographic data. These data can be obtained free of charge from The Cambridge Crystallographic Data Centre.

Preparation of halogen bonding molecular clusters. Experiments were carried out under UHV conditions (10^{-9} mbar). The metal single crystals were cleaned via repeated cycles of Argon sputtering and subsequent annealing to 800 K. 2-TBQP precursors were thermally deposited from a Knudsen effusion cell onto metal substrates held at room temperature. After molecular deposition, the sample was *in-situ* transferred to STM/AFM chamber for imaging at 4.2 K.

Characterization. BR-STM/nc-AFM measurements were carried out an integrated scanning probe system consists of ScientaOmicron low-temperature scanning tunneling microscopy (LT-STM) combined with non-contact atomic force microscopy (nc-AFM). The BR-STM images were recorded in both constant current/height mode using AFM tip with functional CO molecule, and bias voltages were applied to the sample. For nc-AFM images, the constant-height mode with AFM CO-tip was used to record the frequency shift (Δf) of the qPlus resonator (sensor frequecy $f_0 \approx 27000$ Hz, Q ≈ 25000). All the measurements were performed at 4.2 K under a base pressure better than 10^{-11} mbar.

Computational details. All calculations were performed by using Perdew-Burke-Ernzerhof (PBE)[44] electronic interaction as implemented in Vienna *ab initio* package (VASP)[2].[45, 46] The projector augmented wave (PAW)[47] method was used with cut-off energy of 500 eV. A Gamma-point-only *k*-mesh was used for sampling Brillouin zone. All structures were fully relaxed until forces and energy differences were less than 0.05 eV/Å and 10^{-5} eV, respectively. The thickness of vacuum was larger than 12 Å to minimize interactions between periodic images. Van der Waals interactions were introduced by DFT-D2 method.[48] The electrostatic potential was calculated by using Gaussian software within the framework of DFT.

References

(1) Goronzy, D. P.; Ebrahimi, M.; Rosei, F.; Arramel; Fang, Y.; De Feyter, S.; Tait, S. L.; Wang, C.; Beton, P. H.; Wee, A. T. S.; Weiss, P. S.; Perepichka, D. F., Supramolecular Assemblies on Surfaces: Nanopatterning, Functionality, and Reactivity. *ACS Nano* **2018,** *12*, 7445-7481.
(2) Slater, A. G.; Beton, P. H.; Champness, N. R., Two-Dimensional Supramolecular Chemistry on Surfaces. *Chemical Science* **2011,** *2*, 1440-1448.
(3) Yang, Z.; Fromm, L.; Sander, T.; Gebhardt, J.; Schaub, T. A.; Görling, A.; Kivala, M.; Maier, S., On-Surface Assembly of Hydrogen- and Halogen-Bonded Supramolecular Graphyne-Like Networks. *Angew. Chem. Int. Ed.* **2020,** *59*, 9549-9555.
(4) Zhang, Y.-Q.; Paszkiewicz, M.; Du, P.; Zhang, L.; Lin, T.; Chen, Z.; Klyatskaya, S.; Ruben, M.; Seitsonen, A. P.; Barth, J. V.; Klappenberger, F., Complex Supramolecular Interfacial

Tessellation through Convergent Multi-Step Reaction of a Dissymmetric Simple Organic Precursor. *Nat. Chem.* **2018,** *10*, 296-304.

(5) Urgel, J. I.; Écija, D.; Lyu, G.; Zhang, R.; Palma, C.-A.; Auwärter, W.; Lin, N.; Barth, J. V., Quasicrystallinity Expressed in Two-Dimensional Coordination Networks. *Nat. Chem.* **2016,** *8*, 657-662.

(6) Wang, D.; Yang, M.; Arramel; Wu, J.; Wee, A. T. S., Thermally Induced Chiral Aggregation of Dihydrobenzopyrenone on Au(111). *ACS Appl. Mater. Interfaces* **2020,** *12*, 35547-35554.

(7) Barth, J. V., Molecular Architectonic on Metal Surfaces. *Annu. Rev. Phys. Chem.* **2007,** *58*, 375-407.

(8) Otero, R.; Gallego, J. M.; de Parga, A. L. V.; Martín, N.; Miranda, R., Molecular Self-Assembly at Solid Surfaces. *Adv. Mater.* **2011,** *23*, 5148-5176.

(9) Mukherjee, A.; Teyssandier, J.; Hennrich, G.; De Feyter, S.; Mali, K. S., Two-Dimensional Crystal Engineering Using Halogen and Hydrogen Bonds: Towards Structural Landscapes. *Chemical Science* **2017,** *8*, 3759-3769.

(10) Teyssandier, J.; Mali, K. S.; De Feyter, S., Halogen Bonding in Two-Dimensional Crystal Engineering. *ChemistryOpen* **2020,** *9*, 225-241.

(11) Mukherjee, A.; Sanz-Matias, A.; Velpula, G.; Waghray, D.; Ivasenko, O.; Bilbao, N.; Harvey, Jeremy N.; Mali, K. S.; De Feyter, S., Halogenated Building Blocks for 2d Crystal Engineering on Solid Surfaces: Lessons from Hydrogen Bonding. *Chemical Science* **2019,** *10*, 3881-3891.

(12) Wang, D.; Liao, S.; Zhang, S.; Wang, Y., A Reversed Photosynthesis-Like Process for Light-Triggered Co2 Capture, Release, and Conversion. *ChemSusChem* **2017,** *10*, 2573-2577.

(13) Han, Z.; Czap, G.; Chiang, C.-l.; Xu, C.; Wagner, P. J.; Wei, X.; Zhang, Y.; Wu, R.; Ho, W., Imaging the Halogen Bond in Self-Assembled Halogenbenzenes on Silver. *Science* **2017,** *358*, 206-210.

(14) Kawai, S.; Sadeghi, A.; Xu, F.; Peng, L.; Orita, A.; Otera, J.; Goedecker, S.; Meyer, E., Extended Halogen Bonding between Fully Fluorinated Aromatic Molecules. *ACS Nano* **2015,** *9*, 2574-2583.

(15) Lawrence, J.; Sosso, G. C.; Đorđević, L.; Pinfold, H.; Bonifazi, D.; Costantini, G., Combining High-Resolution Scanning Tunnelling Microscopy and First-Principles Simulations to Identify Halogen Bonding. *Nat. Commun.* **2020,** *11*, 2103.

(16) Xing, L.; Jiang, W.; Huang, Z.; Liu, J.; Song, H.; Zhao, W.; Dai, J.; Zhu, H.; Wang, Z.; Weiss, P. S.; Wu, K., Steering Two-Dimensional Porous Networks with Σ-Hole Interactions of Br···S and Br···Br. *Chem. Mater.* **2019,** *31*, 3041-3048.

(17) Kikkawa, Y.; Nagasaki, M.; Koyama, E.; Tsuzuki, S.; Hiratani, K., Hexagonal Array Formation by Intermolecular Halogen Bonding Using a Binary Blend of Linear Building Blocks: Stm Study. *Chem. Commun.* **2019,** *55*, 3955-3958.

(18) Yang, X.-Q.; Yi, Z.-Y.; Wang, S.-F.; Chen, T.; Wang, D., Construction of 2d Extended Cocrystals on the Au(111) Surface Via I···Oaldehyde Halogen Bonds. *Chem. Commun.* **2020,** *56*, 3539-3542.

(19) Zheng, Q.-N.; Liu, X.-H.; Chen, T.; Yan, H.-J.; Cook, T.; Wang, D.; Stang, P. J.; Wan, L.-J., Formation of Halogen Bond-Based 2d Supramolecular Assemblies by Electric Manipulation. *J. Am. Chem. Soc.* **2015,** *137*, 6128-6131.

(20) Shang, J.; Wang, Y.; Chen, M.; Dai, J.; Zhou, X.; Kuttner, J.; Hilt, G.; Shao, X.; Gottfried, J. M.; Wu, K., Assembling Molecular Sierpiński Triangle Fractals. *Nat. Chem.* **2015,** *7*, 389-393.

(21) Wang, D.; Wang, Z.; Liu, W.; Arramel; Zhou, J.; Feng, Y. P.; Loh, K. P.; Wu, J.; Wee, A. T. S., Atomic-Level Electronic Properties of Carbon Nitride Monolayers. *ACS Nano* **2020,** *14*, 14008-14016.

(22) Chen, Y.-C.; Cao, T.; Chen, C.; Pedramrazi, Z.; Haberer, D.; de Oteyza, D. G.; Fischer, F. R.; Louie, S. G.; Crommie, M. F., Molecular Bandgap Engineering of Bottom-up Synthesized Graphene Nanoribbon Heterojunctions. *Nat. Nanotech.* **2015,** *10*, 156-160.

(23) Giessibl, F. J., The Qplus Sensor, a Powerful Core for the Atomic Force Microscope. *Review of Scientific Instruments* **2019,** *90*, 011101.

(24) Giessibl, F. J., Advances in Atomic Force Microscopy. *Reviews of Modern Physics* **2003,** *75*, 949-983.

(25) Zhong, Q.; Li, X.; Zhang, H.; Chi, L., Noncontact Atomic Force Microscopy: Bond Imaging and Beyond. *Surface Science Reports* **2020,** *75*, 100509.

(26) Gross, L.; Mohn, F.; Moll, N.; Liljeroth, P.; Meyer, G., The Chemical Structure of a Molecule Resolved by Atomic Force Microscopy. *Science* **2009,** *325*, 1110-1114.

(27) Gross, L.; Mohn, F.; Moll, N.; Schuler, B.; Criado, A.; Guitián, E.; Peña, D.; Gourdon, A.; Meyer, G., Bond-Order Discrimination by Atomic Force Microscopy. *Science* **2012,** *337*, 1326-1329.

(28) Pavliček, N.; Schuler, B.; Collazos, S.; Moll, N.; Pérez, D.; Guitián, E.; Meyer, G.; Peña, D.; Gross, L., On-Surface Generation and Imaging of Arynes by Atomic Force Microscopy. *Nat. Chem.* **2015,** *7*, 623-628.

(29) Fan, Q.; Martin-Jimenez, D.; Werner, S.; Ebeling, D.; Koehler, T.; Vollgraff, T.; Sundermeyer, J.; Hieringer, W.; Schirmeisen, A.; Gottfried, J. M., On-Surface Synthesis and Characterization of a Cycloarene: C108 Graphene Ring. *J. Am. Chem. Soc.* **2020,** *142*, 894-899.

(30) Ruffieux, P.; Wang, S.; Yang, B.; Sánchez-Sánchez, C.; Liu, J.; Dienel, T.; Talirz, L.; Shinde, P.; Pignedoli, C. A.; Passerone, D.; Dumslaff, T.; Feng, X.; Müllen, K.; Fasel, R., On-Surface Synthesis of Graphene Nanoribbons with Zigzag Edge Topology. *Nature* **2016,** *531*, 489-492.

(31) Sweetman, A. M.; Jarvis, S. P.; Sang, H.; Lekkas, I.; Rahe, P.; Wang, Y.; Wang, J.; Champness, N. R.; Kantorovich, L.; Moriarty, P., Mapping the Force Field of a Hydrogen-Bonded Assembly. *Nat. Commun.* **2014,** *5*, 3931.

(32) Zhang, J.; Chen, P.; Yuan, B.; Ji, W.; Cheng, Z.; Qiu, X., Real-Space Identification of Intermolecular Bonding with Atomic Force Microscopy. *Science* **2013,** *342*, 611-4.

(33) Weiss, C.; Wagner, C.; Temirov, R.; Tautz, F. S., Direct Imaging of Intermolecular Bonds in Scanning Tunneling Microscopy. *J. Am. Chem. Soc.* **2010,** *132*, 11864-11865.

(34) Mishra, S.; Beyer, D.; Eimre, K.; Kezilebieke, S.; Berger, R.; Gröning, O.; Pignedoli, C. A.; Müllen, K.; Liljeroth, P.; Ruffieux, P.; Feng, X.; Fasel, R., Topological Frustration Induces Unconventional Magnetism in a Nanographene. *Nat. Nanotech.* **2020,** *15*, 22-28.

(35) Nguyen, G. D.; Tsai, H.-Z.; Omrani, A. A.; Marangoni, T.; Wu, M.; Rizzo, D. J.; Rodgers, G. F.; Cloke, R. R.; Durr, R. A.; Sakai, Y.; Liou, F.; Aikawa, A. S.; Chelikowsky, J. R.; Louie, S. G.; Fischer, F. R.; Crommie, M. F., Atomically Precise Graphene Nanoribbon Heterojunctions from a Single Molecular Precursor. *Nat. Nanotech.* **2017,** *12*, 1077-1082.

(36) Tschakert, J.; Zhong, Q.; Martin-Jimenez, D.; Carracedo-Cosme, J.; Romero-Muñiz, C.; Henkel, P.; Schlöder, T.; Ahles, S.; Mollenhauer, D.; Wegner, H. A.; Pou, P.; Pérez, R.; Schirmeisen, A.; Ebeling, D., Surface-Controlled Reversal of the Selectivity of Halogen Bonds. *Nat. Commun.* **2020,** *11*, 5630.

(37) Hämäläinen, S. K.; van der Heijden, N.; van der Lit, J.; den Hartog, S.; Liljeroth, P.; Swart, I., Intermolecular Contrast in Atomic Force Microscopy Images without Intermolecular Bonds. *Phys. Rev. Lett.* **2014,** *113*, 186102.

(38) Hapala, P.; Kichin, G.; Wagner, C.; Tautz, F. S.; Temirov, R.; Jelínek, P., Mechanism of High-Resolution Stm/Afm Imaging with Functionalized Tips. *Phys. Rev. B* **2014,** *90*, 085421.

(39) Liu, W.; Luo, X.; Bao, Y.; Liu, Y. P.; Ning, G.-H.; Abdelwahab, I.; Li, L.; Nai, C. T.; Hu, Z. G.; Zhao, D.; Liu, B.; Quek, S. Y.; Loh, K. P., A Two-Dimensional Conjugated Aromatic Polymer Via C–C Coupling Reaction. *Nat. Chem.* **2017,** *9*, 563-570.

(40) van der Heijden, N. J.; Hapala, P.; Rombouts, J. A.; van der Lit, J.; Smith, D.; Mutombo, P.; Švec, M.; Jelinek, P.; Swart, I., Characteristic Contrast in Δfmin Maps of Organic Molecules Using Atomic Force Microscopy. *ACS Nano* **2016,** *10,* 8517-8525.

(41) Desiraju, G. R.; Ho, P. S.; Kloo, L.; Legon, A. C.; Marquardt, R.; Metrangolo, P.; Politzer, P.; Resnati, G.; Rissanen, K., Definition of the Halogen Bond (Iupac Recommendations 2013). *Pure and Applied Chemistry* **2013,** *85*, 1711-1713.

(42) Liu, W.; Loh, K. P., Two-Dimensional Conjugated Polymers Based on C–C Coupling. *Acc. Chem. Res.* **2017,** *50*, 522-526.

(43) Pavliček, N.; Herranz-Lancho, C.; Fleury, B.; Neu, M.; Niedenführ, J.; Ruben, M.; Repp, J., High-Resolution Scanning Tunneling and Atomic Force Microscopy of Stereochemically Resolved Dibenzo[a,H]Thianthrene Molecules. *physica status solidi (b)* **2013,** *250*, 2424-2430.

(44) Perdew, J. P.; Burke, K.; Ernzerhof, M., Generalized Gradient Approximation Made Simple. *Phys. Rev. Lett.* **1996,** *77*, 3865-3868.

(45) Kresse, G.; Hafner, J., Ab Initio Molecular-Dynamics Simulation of the Liquid-Metal–Amorphous-Semiconductor Transition in Germanium. *Phys. Rev. B* **1994,** *49*, 14251.

(46) Kresse, G.; Furthmüller, J., Efficient Iterative Schemes for Ab Initio Total-Energy Calculations Using a Plane-Wave Basis Set. *Phys. Rev. B* **1996,** *54*, 11169-11186.

(47) Blöchl, P. E., Projector Augmented-Wave Method. *Phys. Rev. B* **1994,** *50*, 17953-17979.

(48) Grimme, S., Semiempirical Gga-Type Density Functional Constructed with a Long-Range Dispersion Correction. *J. Comput. Chem.* **2006,** *27*, 1787-1799.

Author contributions

D. W. and Prof. A.T.S. W. proposed and designed the project. D. W. performed the sample preparation and STM/nc-AFM experiments and analyzed the experimental results. D. W., Arramel, Z.S. W. and Prof. A.T.S.W. discussed the data. Z.S. W. and S. Z. performed the first-
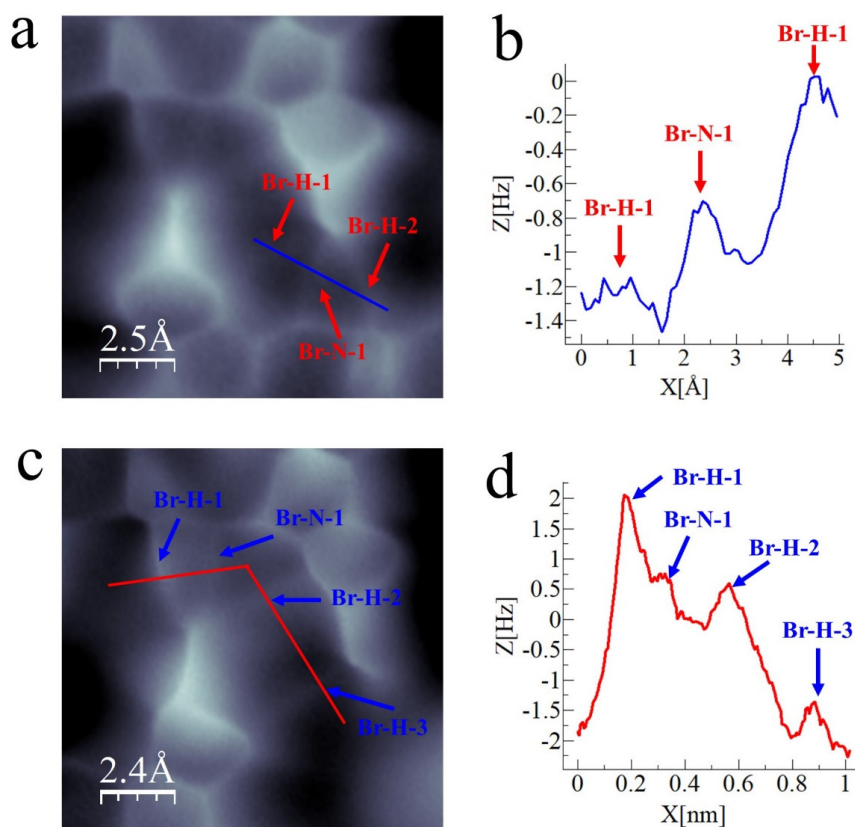
principle calculations. W. L synthesized the molecule precursors. D. W., Arramel, Z. W. and Prof. A.T.S.W. wrote the paper, and all authors discussed and revised the final manuscript.

## Additional information

Supporting Information

**Figure S1**. Bright lines show the formation of Br-H and Br-N halogen bond in type-1 and -2 dimer. (a) High-resolution nc-AFM image of type-1 dimer and (b) its corresponding frequency shift profile, set-point: V= 60 mV, I= 20 pA, tip height Z = -0.2 Å and oscillation amplitude A = 40 pm. (c) High-resolution nc-AFM image of type-2 dimer and (d) its corresponding frequency shift profile, set-point: V=60 mV, I=20 pA, tip height Z = -0.1 Å and oscillation amplitude A = 40 pm. The bright lines between Br-H and Br-N atoms are labeled by arrows, indicating the formation of halogen bonds.
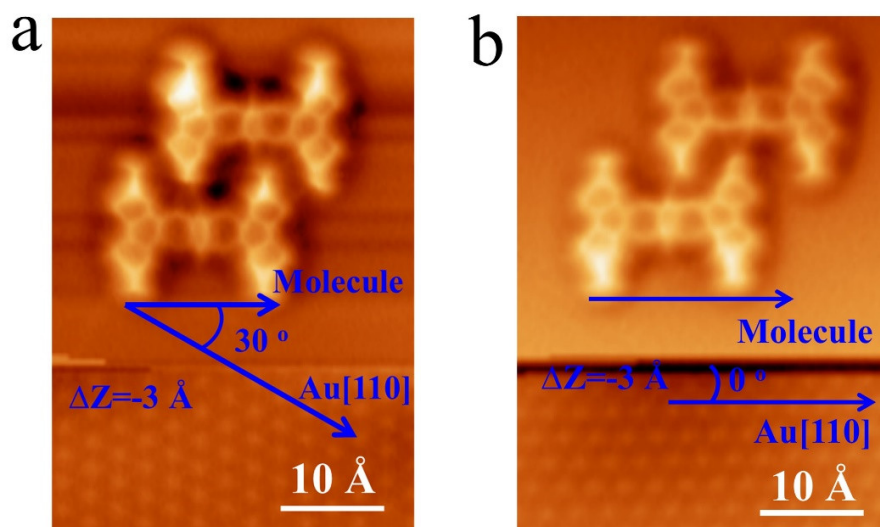
Figure S2. Adsorption alignment of two types of dimers with Au(111) substrate. (a) The nc-AFM image of Br-N halogen bonding type-1 dimer, the alignment angle of type-1 dimer with Au[110] is 30 °. (b) The nc-AFM image of Br-N halogen bonding type-2 dimer, the alignment angle of type-1 dimer with Au[110] is 0 °. The tip sample distance was varied (ΔZ=-3 Å) in order to resolve the adsorption alignment of the two dimers with respect to Au(111) substrate lattice.
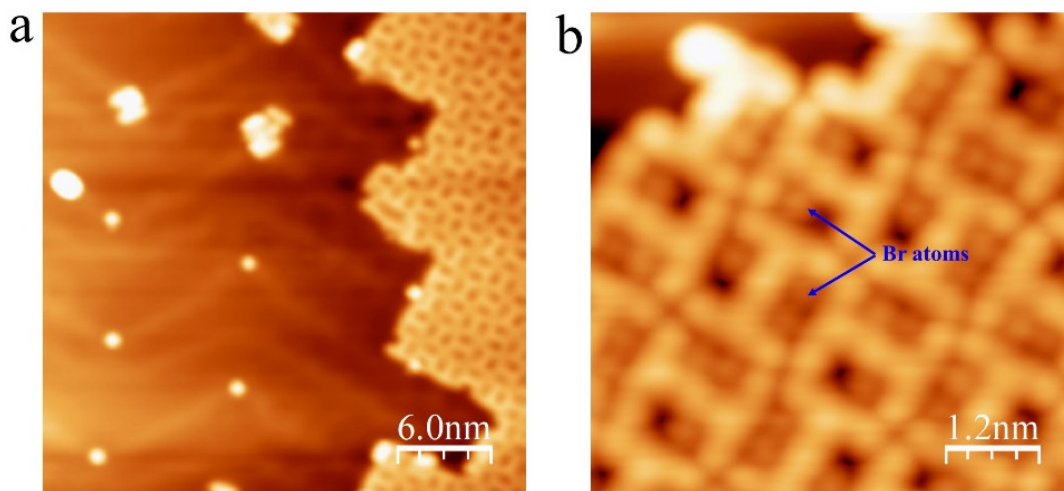
Figure S3. The formation of self-assembled 2-TBQP tetramer assisted by Br atoms absorption. (a) large scale STM image (b) zoom-in STM image of another self-assembled formation of 2-TBQP tetramer on Au(111), set point: a) V = 100 mV and I = 106 pA; b) V=100 mV and I=100 pA, Z=0 Å, the blue arrows indicate the Br-atoms that are adjacent to nitrogen atom sites.
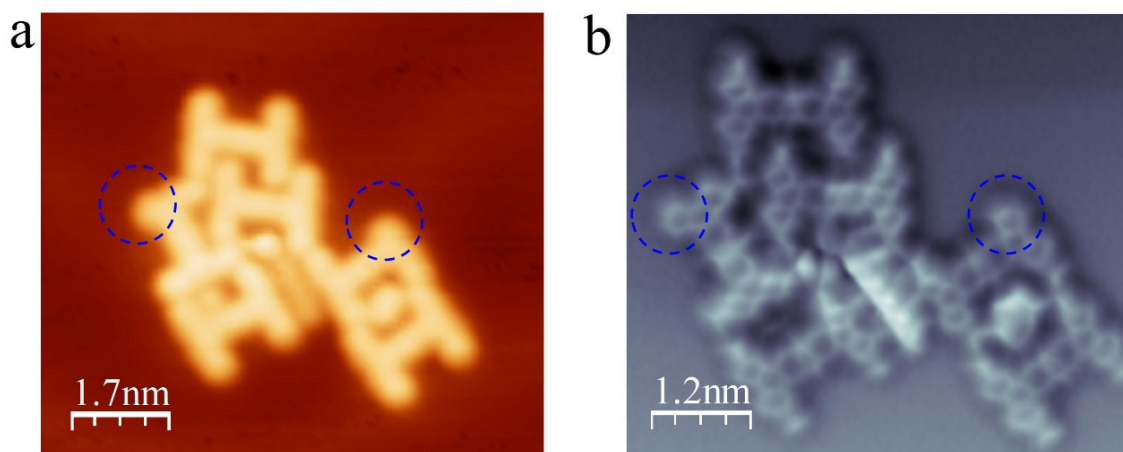
Figure S4. Partial Br-atom cleavage from molecule at room temperature. (a) STM image and (b) nc-AFM image of disorder 2-TBQP molecules on Au(111), set point: a) V = 50 mV and I = 20 pA; b) V= 50 mV, I= 20 pA, tip height Z = 0.3 Å and oscillation amplitude A = 40 pm. The blue circles indicate Br atoms cleavage from benzene rings.
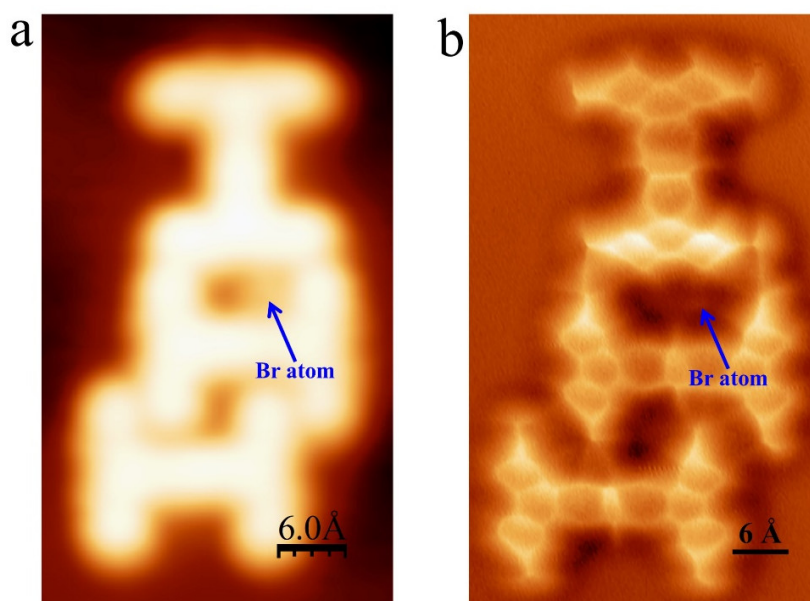
Figure S5. A 2-TBQP trimer stabled by the combination of Br-Br and Br-N halogen bonds. (a) STM image and (b) high-resolution nc-AFM image of a 2-TBQP trimer on Au(111), set point: a) V = 100 mV and I = 20 pA; b) V= 60 mV, I= 20 pA, tip height Z = -0.1 Å and oscillation amplitude A = 40 pm. The blue arrow indicates a Br atom absorption that is adjacent to one nitrogen atom site.
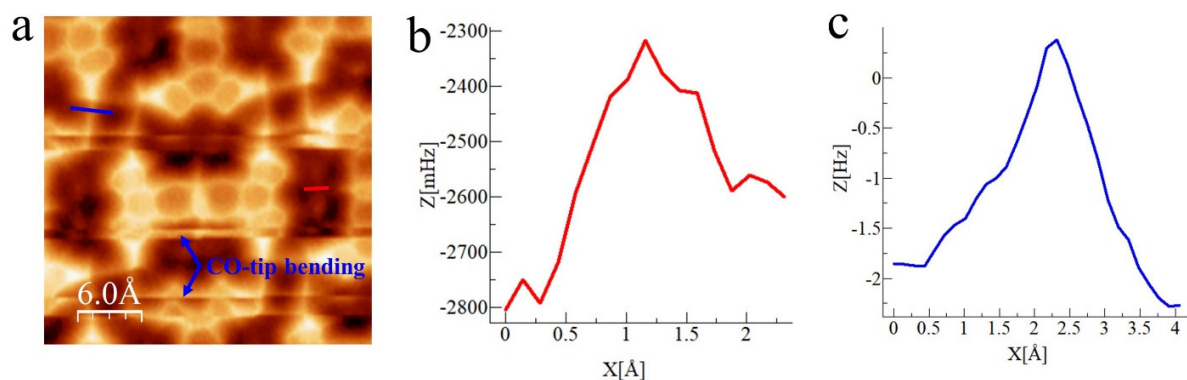
Figure S6. Frequency shift profiles of two adjacent Br-atoms in intermolecular bonding and no bonding cases. (a) High-resolution nc-AFM image of 2-TBQP tetramer at close tip-sample distance, set-point: V= 50 mV, I= 20 pA, tip height Z = -0.3 Å and oscillation amplitude A = 60 pm. (b) The corresponding frequency shift profile of two adjacent Br-atoms in no bonding case (red line in a). (c) The corresponding frequency shift profile of two adjacent Br-atoms in intermolecular bonding case (blue line in a). The disturbed lines are labeled by blue arrows, suggesting CO-tip bending occurs.